



The small k_T region in Drell–Yan production at next-to-leading order with the parton branching method

I. Bujanja^{1,2,a}, A. Bermudez Martinez³, L. Favart^{2,b}, F. Guzman⁴, F. Hautmann^{3,5,6}, H. Jung^{7,8,c},
A. Lelek⁵, M. Mendizabal⁷, K. Moral Figueroa⁷, L. Moureaux^{9,d}, N. Raicevic^{1,e}, M. Seidel¹⁰,
S. Taheri Monfared^{7,f}

¹ Faculty of Science and Mathematics, University of Montenegro, Podgorica, Montenegro
² Interuniversity Institute for High Energies (IIHE), Université libre de Bruxelles, Brussels, Belgium
³ CERN, Geneva, Switzerland
⁴ InSTEC, Universidad de La Habana, Havana, Cuba
⁵ Elementary Particle Physics, University of Antwerp, Antwerp, Belgium
⁶ University of Oxford, Oxford, UK
⁷ Deutsches Elektronen-Synchrotron DESY, Hamburg, Germany
⁸ II. Institut für Theoretische Physik, Universität Hamburg, Hamburg, Germany
⁹ Institut für Experimentalphysik, Universität Hamburg, Hamburg, Germany
¹⁰ Riga Technical University, Riga, Latvia

Received: 15 December 2023 / Accepted: 29 January 2024
© The Author(s) 2024

Abstract The Parton Branching (PB) method describes the evolution of transverse momentum dependent (TMD) parton distributions, covering all kinematic regions from small to large transverse momenta k_T . The small k_T -region is very sensitive both to the contribution of the intrinsic motion of partons (intrinsic k_T) and to the resummation of soft gluons taken into account by the PB TMD evolution equations. We study the role of soft-gluon emissions in TMD as well as integrated parton distributions. We perform a detailed investigation of the PB TMD methodology at next-to-leading order (NLO) in Drell–Yan (DY) production for low transverse momenta. We present the extraction of the nonperturbative “intrinsic- k_T ” distribution from recent measurements of DY transverse momentum distributions at the LHC across a wide range in DY masses, including a detailed treatment of statistical, correlated and uncorrelated uncertainties. We comment on the (in)dependence of intrinsic transverse momentum on DY mass and center-of-mass energy, and on the comparison with other approaches.

1 Introduction

The measurement of the vector boson transverse momentum, p_T , in Drell–Yan (DY) production [1] allows one to investigate in detail many different aspects of the strong interaction sector of the Standard Model, and their impact on precision electroweak measurements. The very low p_T region of the DY cross section is sensitive to the contribution from the non-perturbative transverse motion of partons inside the hadrons; additionally at low transverse momentum multiple soft gluon emissions have to be resummed; at larger transverse momenta perturbative higher-order contributions become dominant. The precise description of the Z/γ boson transverse momentum distribution has been investigated since the 1980’s, and approaches like CSS [2] analytic resummation and parton-shower [3–6] numerical algorithms have been applied with different success.

In this work we explore the approach [7, 8] to DY p_T spectra based on the parton branching (PB) TMD methodology in momentum space proposed in [9, 10], and we perform a detailed analysis of the small- p_T region for wide ranges in center of mass energies and in DY masses. Though fitted only on deep-inelastic scattering (DIS) data from HERA experiments, the PB-TMD methodology has been shown to be capable of describing DY p_T spectra at LHC energies [7] and at low energies [8] without any need for adjustment of parameters. This approach takes into account simultaneously

^a e-mail: itana.bujanja@cern.ch

^b e-mail: Laurent.Favart@ulb.be

^c e-mail: hannes.jung@desy.de (corresponding author)

^d e-mail: louis.moureaux@cern.ch

^e e-mail: nataras@ucg.ac.me

^f e-mail: sara.taheri.monfared@desy.de

soft gluon radiations and the transverse momentum recoils in the parton branchings along the QCD cascade. It provides a successful natural treatment of the multiple-scale problem of the DY transverse momentum for transverse momenta much smaller than DY masses but also of the DY with hard jet production [11]. It also confirms the universality of the TMDs being able to describe both DIS and DY cross sections at all available center of mass energies [12]. Alternative approaches based on parton showers in standard Monte Carlo event generators like PYTHIA8 [3] can also describe multi-differential DY cross section but it has been observed that they require intrinsic transverse momentum distributions strongly dependent on \sqrt{s} [13, 14]. In order to describe the measurements at LHC energies, a Gaussian width exceeding the Fermi motion kinematics is needed. Approaches based on CSS [15] provide very precise analytic predictions for inclusive enough observables like the Drell–Yan cross section transverse momentum. In this paper we study in detail the low k_T behavior of the PB-TMD parton distributions where both very soft gluon emission and intrinsic- k_T contribute significantly and interplay. The results presented here provide a multi-scale economical and coherent approach demonstrating the sensitivity to nonperturbative TMD contributions and first steps in disentangling the intrinsic- k_T contribution from the nonperturbative Sudakov one [16]. We compare DY theoretical predictions with experimental measurements in wide ranges in center-of-mass energies, \sqrt{s} and in DY masses, m_{DY} , to extract the intrinsic- k_T parameter from the transverse momentum distributions. We are carefully taking into account systematic and statistical uncertainties using the breakdown of experimental uncertainties provided by the full set of covariance matrices available in the recent Drell–Yan differential cross section measurement at 13 TeV [17] and we treat for the first time the scale uncertainties in the theoretical predictions as correlated uncertainties within a given mass bin.

The results for TMD parameters such as intrinsic- k_T obtained from the DY analysis in this paper can be compared with analogous results obtained from TMD fits in the CSS coordinate-space framework, see e.g. the recent studies [18, 19]. A significant difference between these approaches and the approach of this paper concerns the treatment of collinear parton distribution functions (PDFs). As shown in Refs. [7, 8], in the approach of this paper the inclusive DGLAP limit is recovered and fits of collinear distributions are made, e.g. from inclusive DIS structure functions, along with TMD distributions [20–22]. In contrast, CSS approaches do not recover inclusive DGLAP and rather use an ansatz based on the operator product expansion of TMD distributions in terms of collinear PDFs, assuming collinear PDFs to be given by standard PDF sets. The PDF bias effect [19] which results from this has been shown to influence significantly the central values of the extracted distributions

and dominate the systematic uncertainties in all the existing TMD determinations based on CSS approaches. The possibility to treat collinear and TMD distributions on the same footing and determine them without having to rely on existing PDF fits is a distinctive feature of the PB TMD approach. We believe that in the long run this could bring significant advantages in pursuing TMD phenomenology.

On the other hand, the results of this paper for intrinsic- k_T can also be compared with the case of parton shower Monte Carlo event generators, such as PYTHIA [3] and HERWIG [4]. Monte Carlo tuning to experimental data shows that parton shower approaches require intrinsic- k_T distributions dependent on the center-of-mass energy \sqrt{s} [13, 14], and a Gaussian width exceeding the Fermi motion kinematics. In contrast, in the approach of this paper we find that the width of the intrinsic- k_T distribution has a much milder center-of-mass energy \sqrt{s} dependence. We obtain more natural Gaussian width σ , $\sigma = q_s/\sqrt{2}$, with q_s close to 1 GeV resulting from fits to DY measurements from fixed-target to LHC energies. We propose in this paper that the different behavior, concerning intrinsic- k_T distributions, between PB TMD and parton-shower approaches can be ascribed to the different treatment of the contributions to parton evolution from the nonperturbative Sudakov region, near the soft-gluon resolution boundary. See also [23] for a discussion of this and comparison of PB TMD and parton-shower results.

The paper is organized as follows. In Sect. 2 we briefly recall the basic elements of the calculational framework [7, 9, 10, 21–23]: we start with the PB TMD approach; next we give a few comments on the treatment of the small transverse momentum region in this approach; then we discuss the Monte Carlo computation of DY differential distributions. Section 3 is the central section of the paper, in which we perform fits to DY data and present results for the intrinsic- k_T TMD parameter. We give conclusions in Sect. 4.

2 PB TMDs and DY production

To study the different contributions to the low- p_T spectrum, at different m_{DY} and different \sqrt{s} , we calculate DY production cross section in the PB TMD method, which proceeds as described in Refs. [7, 23]. NLO hard-scattering matrix elements are obtained from the MADGRAPH5_AMC@NLO [24] next-to-leading (NLO) event generator and matched with TMD parton distributions and showers obtained from PB evolution [9, 10, 20], using the subtractive matching procedure proposed in [7] and further analyzed in [25].

We will show that the application of PB TMD distributions leads to a non negligible contribution of pure intrinsic- k_T , even if most of the small- k_T contribution comes from the PB-evolution. We also show that the proper treatment of photon radiation from the DY decay leptons is rather impor-

tant, especially in the DY mass region below the Z boson peak. The contribution of intrinsic- k_T of heavy flavor partons is found to be negligible over the whole range since heavy quarks are not present in the initial configuration of the proton.

2.1 TMD distributions from the PB method

The PB evolution equations for TMD parton distributions $\mathcal{A}_a(x, \mathbf{k}, \mu^2)$ of flavor a are given by [9]

$$\begin{aligned} \mathcal{A}_a(x, \mathbf{k}, \mu^2) &= \Delta_a(\mu^2) \mathcal{A}_a(x, \mathbf{k}, \mu_0^2) \\ &+ \sum_b \int \frac{d^2 \mathbf{q}'}{\pi \mathbf{q}'^2} \frac{\Delta_a(\mu^2)}{\Delta_a(\mathbf{q}'^2)} \Theta(\mu^2 - \mathbf{q}'^2) \Theta(\mathbf{q}'^2 - \mu_0^2) \\ &\times \int_x^{z_M} \frac{dz}{z} P_{ab}^{(R)}(\alpha_s, z) \mathcal{A}_b\left(\frac{x}{z}, \mathbf{k} + (1-z)\mathbf{q}', \mathbf{q}'^2\right), \end{aligned} \tag{1}$$

where \mathbf{k} and \mathbf{q} are 2-dimensional momentum vectors, z_M is the soft resolution scale [10], z is the longitudinal momentum transferred at the branching, $P_{ab}^{(R)}(\alpha_s, z)$ are the resolvable splitting functions¹ (whose explicit expressions for all flavor channels are given in [9]), and Δ_a are the Sudakov form factors

$$\begin{aligned} \Delta_a(z_M, \mu^2, \mu_0^2) &= \exp\left(-\sum_b \int_{\mu_0^2}^{\mu^2} \frac{d\mathbf{q}'^2}{\mathbf{q}'^2} \int_0^{z_M} dz z P_{ab}^{(R)}(\alpha_s, z)\right). \end{aligned} \tag{2}$$

The branching evolution (1) fulfills soft-gluon angular ordering [27–29], with the branching variable \mathbf{q}'^2 being related to the transverse momentum q_T of the parton emitted at the branching by

$$q_T = (1-z)|\mathbf{q}'|. \tag{3}$$

It is shown in [10] that angular ordering is essential for the TMD distribution arising from the solution of Eq. (1) to be well-defined and independent of the choice of the soft-gluon resolution scale $z_M = 1 - \varepsilon$ for $\varepsilon \rightarrow 0$. In contrast, p_T ordering leads, for instance, to ambiguities in the definition of the TMD from the $z \rightarrow 1$ region.

Analogously to the case of ordinary (collinear) parton distribution functions, the distribution $\mathcal{A}_a(x, \mathbf{k}, \mu_0^2)$ at the starting scale μ_0 of the evolution, in the first term on the right hand side of Eq. (1), is a nonperturbative boundary condition to the evolution equation, and is to be determined from experimental data. For simplicity we parameterize $\mathcal{A}_a(x, \mathbf{k}, \mu_0^2)$ in the form

$$\mathcal{A}_{0,a}(x, \mathbf{k}, \mu_0^2) = f_{0,a}(x, \mu_0^2) \cdot \exp\left(-|\mathbf{k}|^2/2\sigma^2\right)/(2\pi\sigma^2), \tag{4}$$

¹ Using transverse momentum dependent splitting functions as described in Ref. [26] would require using off-shell matrix elements and a completely new fit to inclusive structure functions.

with the width of the Gaussian distribution given by $\sigma = q_s/\sqrt{2}$, independent of parton flavor and x , where q_s is the intrinsic- k_T parameter.

The scale at which the strong coupling α_s is to be evaluated in Eqs. (1) and (2) is a function of the branching variables. Two scenarios are studied in Refs. [9, 20]:

- i) : $\alpha_s = \alpha_s(\mathbf{q}'^2)$
- ii) : $\alpha_s = \alpha_s(\mathbf{q}'^2(1-z)^2) = \alpha_s(q_T^2)$ (5)

In scenario i), it is shown in [9] that Eq. (1), in the collinear case, i.e. once it is integrated over all transverse momenta, reproduces exactly the DGLAP evolution [30–33] of parton densities. In scenario ii), it is discussed in [34] how, upon integration over transverse momenta and suitable treatment of the resolution scale, Eq. (1) returns the CMW coherent branching evolution [29].

In Ref. [20], fits to precision DIS HERA measurements [35] based on Eqs. (1) and (4), combined with NLO DIS matrix elements, are performed for both scenarios i) and ii), using the fitting platform xFitter [36, 37]. It is found that fits to DIS measurements with good χ^2 values can be achieved in either case. Correspondingly, PB-NLO-HERAI+II-2018 set 1 (abbreviated as PB-NLO-2018 Set1) (with the DGLAP-type $\alpha_s(\mathbf{q}'^2)$) and PB-NLO-HERAI+II-2018 set2 (abbreviated as PB-NLO-2018 Set2) (with the angular-ordered CMW-type $\alpha_s(q_T^2)$) are obtained, both having intrinsic- k_T parameter in Eq. (4) set to $q_s = 0.5$ GeV [20]. All PB TMD parton distributions (and many others) are accessible in TMDlib and via the graphical interface TMD-plotter [38, 39].

On the other hand, it is found that PB-NLO-2018 Set2 provides a much better description, compared to PB-NLO-2018 Set1, of measured Z/γ transverse momentum spectra at the LHC [7], in low-energy experiments [23], and of dijet azimuthal correlations near the back-to-back region at the LHC [40]. This underlines the relevance of the angular-ordered coupling $\alpha_s(q_T^2)$ in regions dominated by soft-gluon emissions.

Based on this observation, in the following we will focus on the PB-NLO-2018 Set2 approach and perform fits to DY transverse momentum measurements to investigate the sensitivity of these measurements to the nonperturbative TMD intrinsic- k_T parameter q_s , and perform determinations of its value.

As discussed in [7, 20], in order to complete the definition of the PB-NLO-2018 Set2 scenario the treatment of the coupling α_s needs to be specified in the region of small transverse momenta $q_T \lesssim q_0$, where q_0 is a semi-hard scale on the order of a GeV. As in [7, 20], we take

$$\alpha_s = \alpha_s(\max(q_0^2, q_T^2)), \tag{6}$$

setting $q_0 = 1$ GeV, which may be regarded as similar in spirit to the “pre-confinement” proposal in the context of infrared-sensitive QCD processes [41, 42].² In the present study, we will perform a determination of the nonperturbative TMD parameter q_s from DY transverse spectra by assuming the above behavior for α_s .

To better illustrate the underlying physical picture, we give next a few further comments on nonperturbative contributions and the treatment of the small transverse momentum region in the PB TMD approach.

As implied by Eqs. (1) and (2), the PB TMD method incorporates Sudakov evolution via phase space integrations of appropriate kernels over the resolvable region, i.e. over momentum transfers z up to the soft-gluon resolution scale z_M . For each branching evolution scale \mathbf{q}'^2 , it is instructive to examine separately parton emissions with transverse momenta above the semi-hard scale q_0 , $q_T > q_0$, and below q_0 , $\Lambda_{\text{QCD}} < q_T \lesssim q_0$. Using the angular ordering relation (3), these emissions are mapped respectively on the regions

$$\begin{aligned} (a) : \quad & z < z_{\text{dyn}} = 1 - q_0/|\mathbf{q}'|, \\ (b) : \quad & z_{\text{dyn}} \lesssim z < z_M, \end{aligned} \quad (7)$$

where $z_{\text{dyn}} = 1 - q_0/|\mathbf{q}'|$ is the dynamical resolution scale associated with the angular ordering [27–29, 34]. In region (a), the strong coupling (6) is evaluated at the scale of the emitted transverse momentum, $\alpha_s(q_T^2)$; the contribution from region (a) to the evolution in Eqs. (1), (2) corresponds to the perturbative Sudakov resummation (see e.g. [43, 44]). In region (b), the strong coupling (6) freezes around the semi-hard scale q_0 ; the contribution from region (b) to the evolution is the nonperturbative Sudakov form factor in the PB TMD approach.

It is worth noting that the PB-NLO-2018 Set 2 framework provides a very natural and economical description of nonperturbative Sudakov effects, based on perturbative modeling of the Sudakov form factor (2) combined with the infrared α_s behavior (6): it does not contain any additional nonperturbative functions and parameters, besides the scale q_0 .

In Fig. 1 we show parton distributions obtained with the PB approach using the starting distributions from PB-NLO-2018 Set2. We show distributions for the gluon and down quark parton densities for different values of z_M : $z_M \rightarrow 1$ (default - regions (a + b) - red curve [20]) and $z_M = z_{\text{dyn}} = 1 - q_0/|\mathbf{q}'|$ (region (a) only - blue curve obtained with the same parameters as PB-NLO-2018 Set2 except z_M using UPDFEVOLV [45]). The distributions obtained from PB-NLO-2018 set2 with $z_M \rightarrow 1$ are significantly different from those applying $z_M = z_{\text{dyn}}$, illustrating the importance of soft contributions even for collinear distributions. In Ref.

[46] it was found that limiting the z -integration leads to inconsistencies. In Ref. [47] a procedure to correct the z limitation is discussed. A detailed discussion on the role of soft gluons and the nonperturbative Sudakov form factor is given in Ref. [48]. Please note that the intrinsic- k_T distribution, since not part of the collinear calculation, does not affect the collinear parton densities.

In the transverse momentum distributions obtained with the PB-approach, the effect of the z_M cut-off is even more visible. In Fig. 2 the transverse momentum distributions obtained for down and charm quarks are shown for PB-NLO-2018 Set2, with $z_M \rightarrow 1$, i.e. regions (a + b), with (red curve) and without intrinsic- k_T distribution applied (blue curve – a Gauss distribution with $q_s = 0.00001$ GeV). We also show the transverse momentum distribution contribution from region (a) alone, i.e. for $z_M = z_{\text{dyn}} = 1 - q_0/\mu'$, without intrinsic- k_T (corresponding to the magenta curve of Fig. 1). The importance of the large z -region on the transverse momentum distributions is seen in the comparison with the predictions without intrinsic- k_T distribution (blue and magenta curves).

The transverse momentum distributions show very clearly the large effect of the choice of z_M for the soft region, while in the perturbative region $k_T > q_0$ the effect becomes smaller with increasing k_T . Applying such a scale, $z_M = z_{\text{dyn}} = 1 - q_0/\mu'$, removes emissions with $q_T < q_0$ (there are still low- k_T contributions, which come from adding vectorially all intermediate emissions). However, very soft emissions are automatically included with $z_M \rightarrow 1$.

As shown in Fig. 2, the effect of the intrinsic- k_T distribution is much reduced at large scales, but the contribution of the region $z_{\text{dyn}} < z < 1$ stays important for small k_T .

It is interesting to observe that the charm density shows essentially no effect of an intrinsic- k_T distribution: this is because charm is generated dynamically from gluons only, and there is no intrinsic charm density.

2.2 Transverse momentum distributions of PB-NLO-2018

After having discussed the importance of the soft nonperturbative region to the transverse momentum distribution, we turn now to a discussion of the transverse component of the PB parton distributions of Ref. [20], which are used for comparison with measurements.

In previous investigations on Z -boson production at the LHC [7], as well as for low DY mass, m_{DY} , and at low \sqrt{s} [8], it was found that PB-NLO-2018 Set2 describes the measurements much better, while PB-NLO-2018 Set 1 gives too large a cross section at small DY lepton pair transverse momenta, $p_T(\ell\ell)$.

The difference between PB-NLO-2018 Set1 and Set2, which comes from the choice of renormalization scale (argument in α_s), is seen essentially in the low- k_T region, where the

² Different forms of the extension to small q_T could be considered. However, this will entail new fits both to precision DIS data and to DY data.

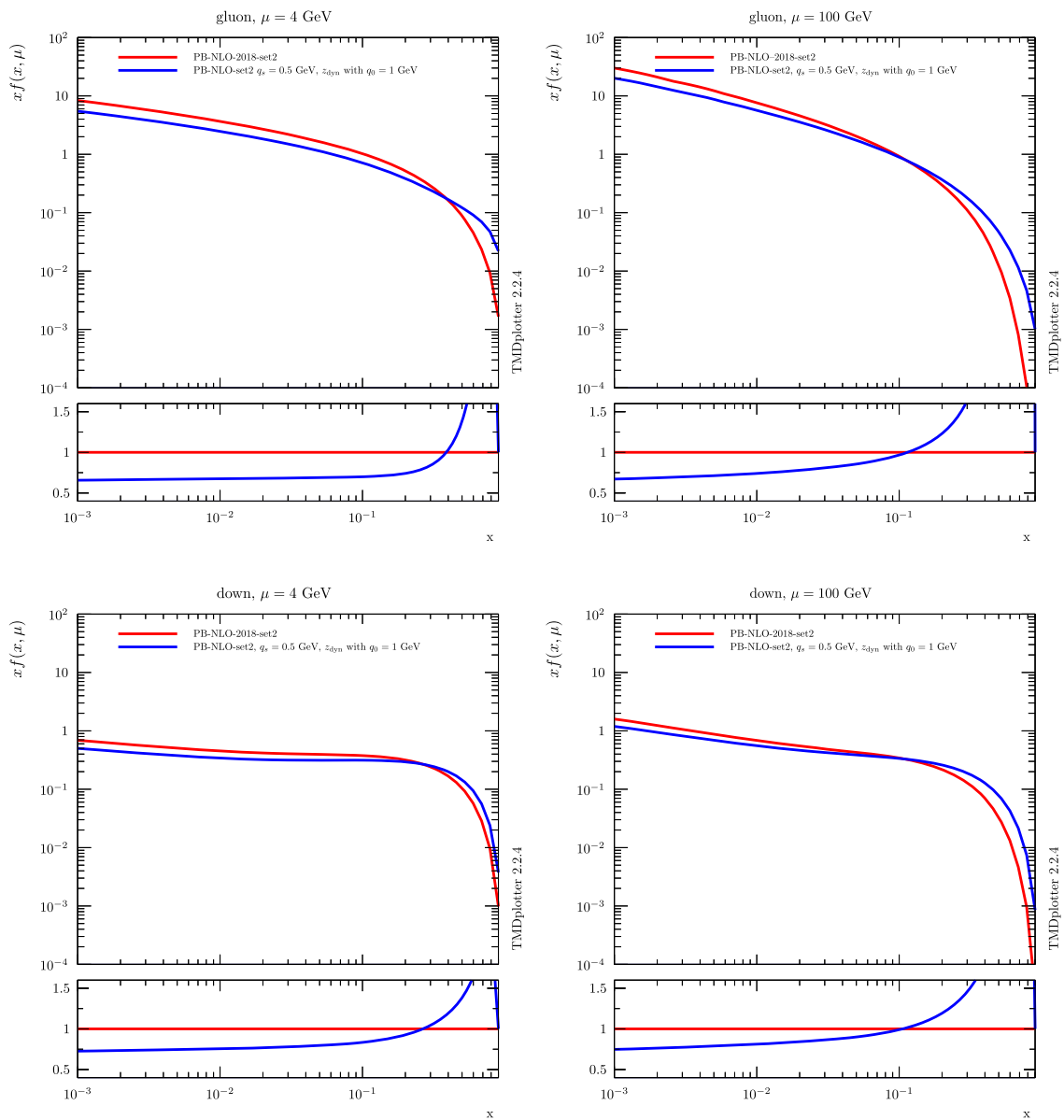


Fig. 1 Integrated gluon and down-quark distributions at $\mu = 4$ GeV (left column) and $\mu = 100$ GeV (right column) obtained from the PB approach based on PB-NLO-2018 Set2. The red curve is the published

PB-NLO-2018 Set2 [20] and corresponds to $z_M \rightarrow 1$ (regions (a + b) in text). The blue curve corresponds to $z_M = z_{\text{dyn}}$ with $q_0 = 1$ GeV (region (a) only). The ratio plots show the ratios to the one for $z_M \rightarrow 1$

nonperturbative Sudakov form factor (region (b)), with the integral $z_M \rightarrow 1$, plays an important role. In Fig. 3 (upper row) the distributions for up and charm quarks are shown when no intrinsic- k_T distribution is included, the lower row shows distributions including the default intrinsic Gauss k_T distributions of widths $q_s = 0.5$ GeV. It is very interesting to observe that the differences between the sets setting $q_s = 0$ or not are very much reduced for heavy flavors since they are only generated dynamically (since heavy flavors are not present at the starting scale in the VFNS which is applied here). In principle an intrinsic charm contribution can be

included in PB densities, however, this is not required from inclusive DIS data [35] used in the fit of PB-NLO-2018 Set2.

In Fig. 4 the transverse momentum distribution for down quarks, with and without an intrinsic- k_T distribution, is shown at different scales μ . While at low scales $\mu \sim 50$ GeV a significant effect of the intrinsic- k_T distribution is observed for very small k_T , at large scales $\mu \sim 350$ GeV this effect is much reduced. This scale dependence will result in a much smaller sensitivity to the intrinsic- k_T distribution at high m_{DY} .

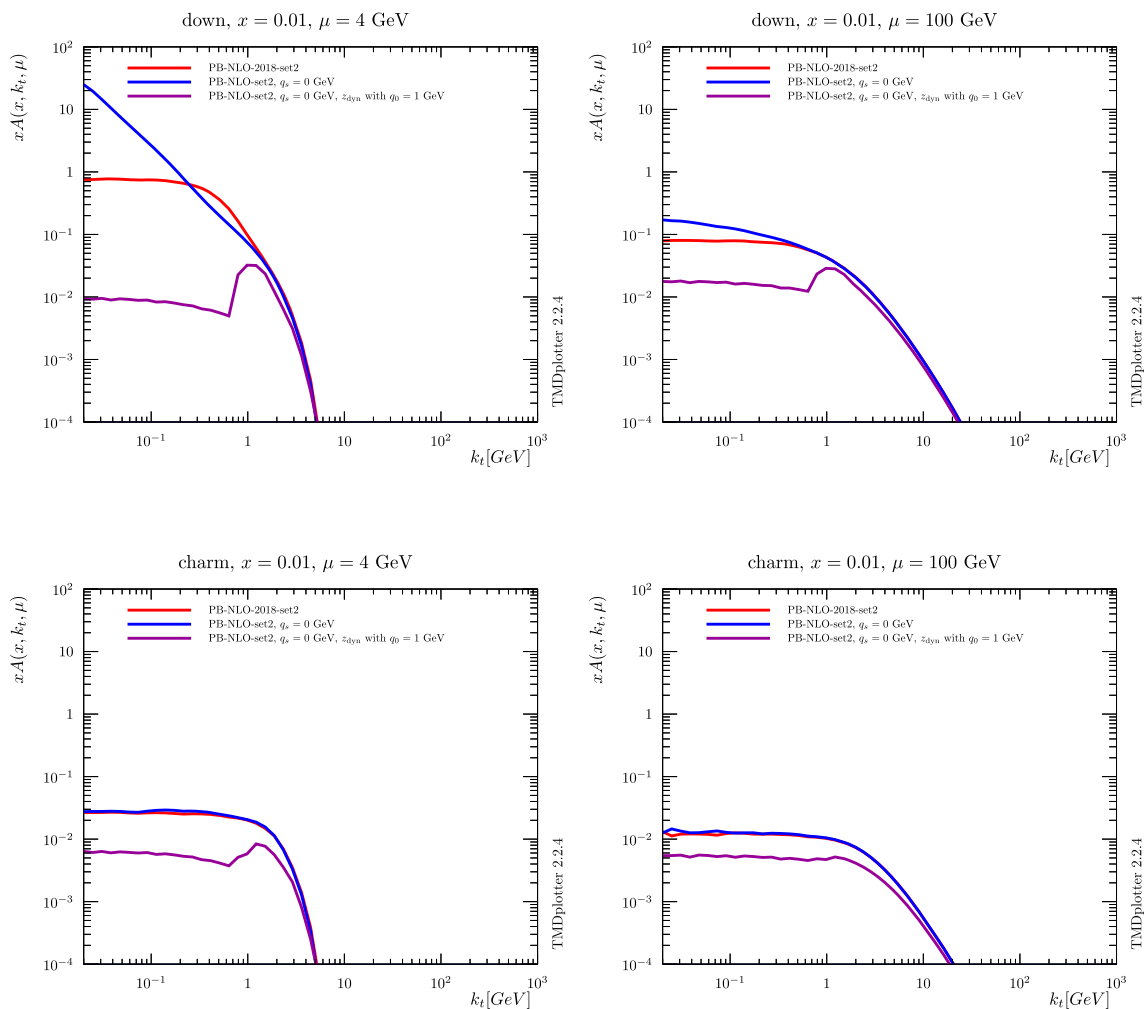


Fig. 2 Transverse momentum distributions of down and charm quarks at $\mu = 4$ GeV (left column) and $\mu = 100$ GeV (right column) obtained from the PB approach based on PB-NLO-2018 Set2. Two distributions do not include intrinsic- k_T : the blue curve corresponds to $z_M \rightarrow 1$

(regions a+b in text) and the magenta curve to $z_M = z_{\text{dyn}} = 1 - q_0/q$ (region a only). The red curve is the published one PB-NLO-2018 Set2 [20] and including intrinsic- k_T and $z_M \rightarrow 1$

2.3 Calculation of the DY cross section

The cross section of DY production is calculated at NLO with MADGRAPH5_AMC@NLO[24]. In the MCatNLO method, the collinear and soft contributions of the NLO cross section are subtracted, as they will be later included when parton shower, or as in our case, TMD parton densities are applied. As in earlier studies, we use CASCADE3 [49] to include TMD parton distributions and parton shower to the MCatNLO calculation (a detailed investigation of the effect of TMD parton distributions and parton showers applied in the CASCADE3 Monte Carlo generator is given in Ref. [25]). We use the HERWIG6 subtraction terms in MCatNLO, since they are based on the same angular ordering conditions as the PB-TMD parton distribution sets, PB-NLO-2018 Set1 and PB-NLO-2018 Set2, described in the previous section. The validity and consistency using HERWIG6 subtraction terms

in MCatNLO together with PB TMD distributions has been studied in detail in the appendix of Ref. [25]. The predicted cross sections (labeled as MCatNLO+CAS3 in the following) are calculated using the integrated versions of the NLO parton densities PB-NLO-2018 Set1 and PB-NLO-2018 Set2 together with $\alpha_s(m_Z) = 0.118$ at NLO.

The factorization scale μ , used in the calculation of the hard process is set to $\mu = \frac{1}{2} \sum_i \sqrt{m_i^2 + p_{T,i}^2}$, with the sum running over all final state particles, in case of DY production over all decay leptons and the final jet. For the generation of transverse momentum according to the PB-TMD distributions, the factorisation scale μ in the hard process is set to $\mu = m_{\text{DY}}$, in the case of a real emission it is set to $\mu = \frac{1}{2} \sum_i \sqrt{m_i^2 + p_{T,i}^2}$. The generated transverse momentum is limited by the matching scale $\mu_m = \text{SCALUP}$ [49]. Since there are no PB-fragmentation functions available yet,

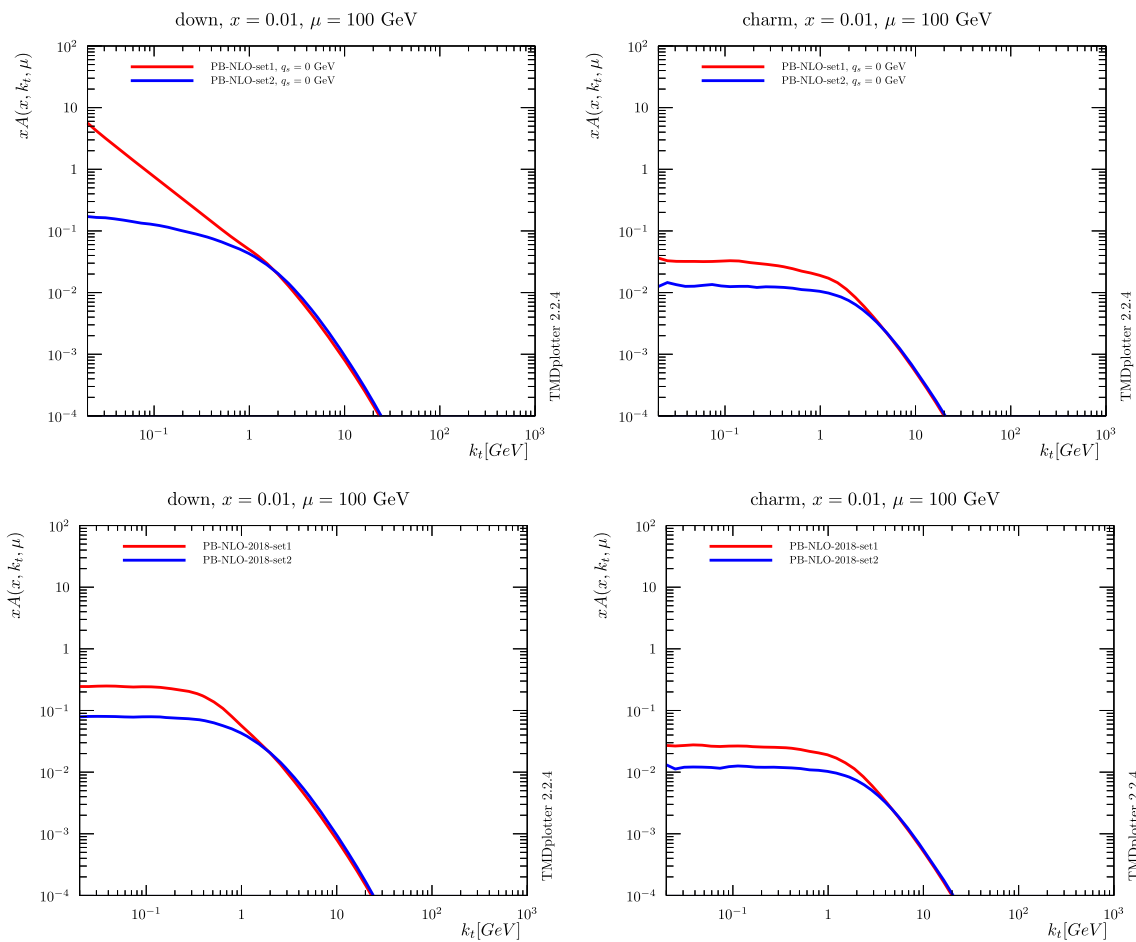


Fig. 3 TMD parton density distributions for down and charm quarks of the published PB-NLO-2018 Set1 (red curve) and PB-NLO-2018 Set2 (blue curve) [20] as a function of k_T at $\mu = 100$ GeV and $x = 0.01$. In

the upper row are shown distributions when no intrinsic- k_T distribution is included ($q_s = 0.00001$ GeV), and the lower row shows the default distributions with $q_s = 0.5$ GeV

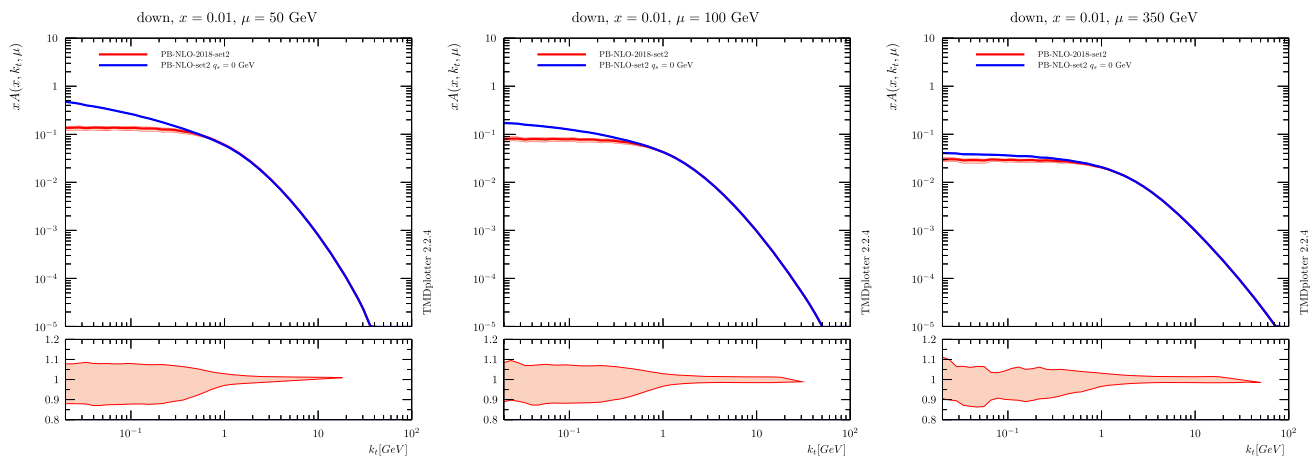


Fig. 4 TMD parton density distributions for down quarks of PB-NLO-2018 Set2 with (red curve) and without (blue curve) intrinsic- k_T distribution as a function of k_T at different scales μ and $x = 0.01$. The lower panels show the full uncertainty of the TMD PDFs, as obtained from the

fits [20]. Shown is the ratio to each central value. The red band shows the uncertainty of PB-NLO-2018 Set2, the blue line has no uncertainty band

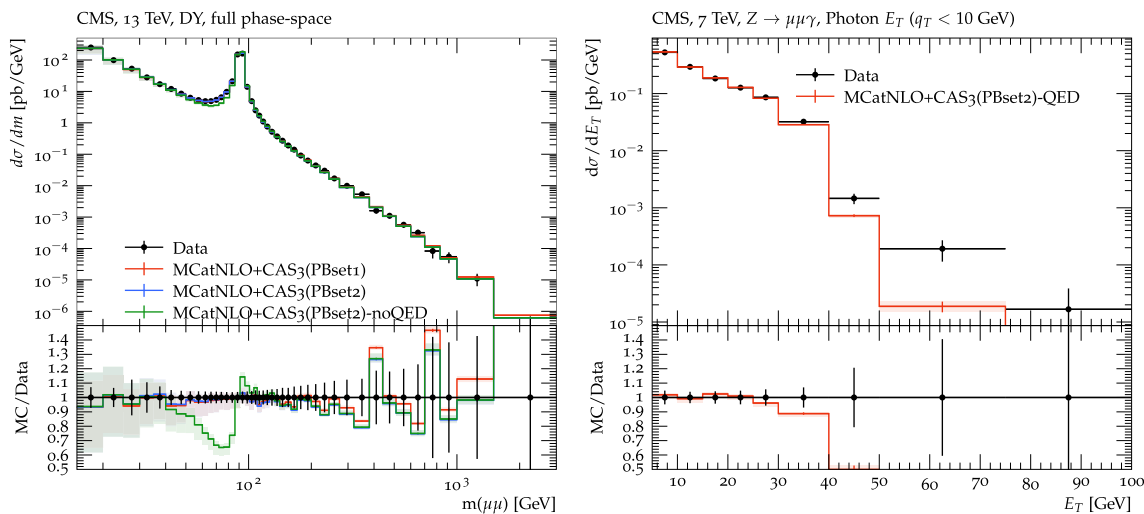


Fig. 5 Left: The mass distribution of DY lepton pairs at 13 TeV [51] compared to predictions of MCatNLO+CAS3 with PB-NLO-2018 Set1 (red curve), PB-NLO-2018 Set2 (blue curve) and without QED corrections (green curve). Right: The spectrum of photons transverse momen-

tum in $Z \rightarrow \mu^+ \mu^- \gamma$ at 7 TeV [55] compared to MCatNLO+CAS3 PB-NLO-2018 Set2 including QED radiation for a transverse momentum of the DY pair $p_T(\ell\ell) < 10$ GeV. The bands show the scale uncertainty

the final state parton shower in CASCADE3 is generated from PYTHIA[50], including photon radiation of the lepton pair.

A good description of the final state QED corrections, and in particular the kinematic effect of the real photon radiations, is essential in order to achieve a precise description of the DY transverse momentum. Figure 5 (left) shows the DY mass distribution as measured by CMS [51] at 13 TeV together with predictions of MCatNLO+CAS3.³ The bands show the scale uncertainty coming from a variation of the renormalization and factorization scale by a factor of two up and down, avoiding the extreme values (7-point variation). The DY mass is calculated from the so-called *dressed-leptons* (see for example [53,54]), where photons radiated within a cone of radius of $R < 0.1$ are merged to the lepton before the momenta are calculated. We show predictions based on PB-NLO-2018 Set1 and Set2, and also, for illustration, when photon radiation is turned off in the final-state shower (labeled as "noQED"). A rather good description of the DY mass spectrum over a large range on m_{DY} is obtained both with PB-NLO-2018 Set1 and Set2. Only at m_{DY} greater than a few hundred GeV the predictions tend to become smaller than the measurement (while still within the uncertainties). However, this is the region where the partonic x becomes large and not well constrained by the fit to HERA data [35] used for the PB-NLO-2018 TMD extraction [20]. In the region of m_{DY} below the Z -pole, one can observe the importance of QED corrections. In Fig. 5 (right) we show the photon transverse momentum spectrum in Z -production as measured by CMS [55] at 7 TeV in comparison

with MCatNLO+CAS3 including QED radiation. The photon spectrum is well described at low $E_T < 40$ GeV, while the high E_T spectrum predicted by the parton shower falls below the measurement, since the precision of parton showers are limited for the high p_T region.

3 The transverse momentum spectrum of DY lepton pairs

The transverse momentum spectrum of DY pairs at $\sqrt{s} = 13$ TeV has been measured for a wide m_{DY} range by CMS [17]. We use this measurement for comparison with predictions of MCatNLO+CAS3 based on PB-NLO-2018 Set1 and PB-NLO-2018 Set2, as shown in Fig. 6. As already observed in previous investigations [7,23,25,40], the PB-NLO-2018 Set1 gives too high a contribution at small transverse momenta $p_T(\ell\ell)$, while PB-NLO-2018 Set2 describes the measurements rather well, without any further adjustment of parameters,⁴ underlining the role of evaluating the strong coupling at the transverse momentum scale. In order to illustrate the importance of QED corrections, we show in addition a prediction based on PB-NLO-2018 Set2 without including QED final state radiation (labeled noQED). Especially in the low m_{DY} region, the inclusion of QED radiation is essential, not only changing the total cross section but rather strongly modifying the shape of the transverse momentum distribu-

³ We use the Rivet package [52] for the calculation of the final distributions.

⁴ The predictions shown here are slightly different compared to the predictions in [17] because we use here a lower minimum k_T cut and because of a bug in the treatment of QED radiation in Rivet, corrected in version 3.1.8.

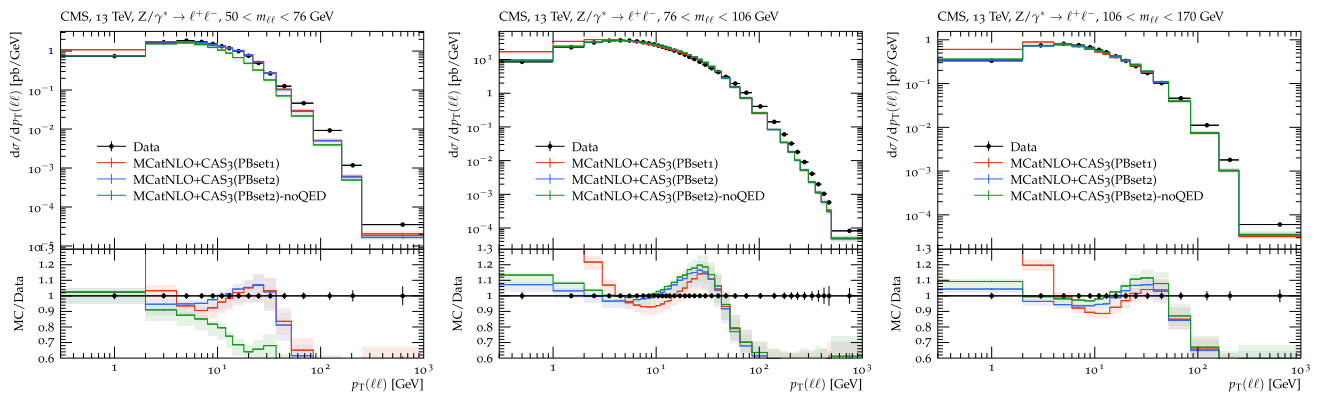


Fig. 6 The $p_T(\ell\ell)$ dependent DY cross section for different m_{DY} regions as measured by CMS [17] compared to MCatNLO+CAS3 predictions based on PB-NLO-2018 Set 1 (red curve) and Set 2 (blue

curve). Also shown are predictions without the inclusion of final state QED radiation from the leptons (green curve). The band shows the 7-point variation of the renormalization and factorization scales

tion $p_T(\ell\ell)$. All calculations predict too low a cross section at large transverse momentum due to missing higher-order contributions in the matrix element. In Refs. [11,56,57] it is shown explicitly that including higher orders in the matrix element through the TMD multi-jet merging technique gives an excellent description even for largest $p_T(\ell\ell)$. For all further distributions, we restrict the investigations to $p_T(\ell\ell)$ below the peak region (i.e. $p_T(\ell\ell) \lesssim 8$ GeV).

3.1 Influence of the intrinsic- k_T distribution on DY transverse momentum distributions

Given the rather successful description of the DY $p_T(\ell\ell)$ -spectrum with MCatNLO+CAS3 using PB-NLO-2018 Set 2 in the low $p_T(\ell\ell)$ -region, we investigate below the importance of the intrinsic- k_T distribution. In PB-NLO-2018 the intrinsic- k_T distribution is parameterized as a Gauss distribution with zero mean and a width $\sigma^2 = q_s^2/2$ [20] (see Eq. (4)), where q_s was fixed by default at $q_s = 0.5$ GeV.

In order to illustrate the sensitivity range of the intrinsic- k_T distribution, we show in Fig. 7 the MCatNLO+CAS3 predictions for the low $p_T(\ell\ell)$ -spectrum of DY production at different DY masses m_{DY} for different intrinsic- k_T distribution (with different q_s parameter values) compared to the CMS measurement [17]. We observe that sensitivity to intrinsic- k_T is more pronounced at small $p_T(\ell\ell)$ values. This sensitivity decreases with increasing mass, as expected from Fig. 4

In the following we describe a determination of the Gaussian width q_s for different DY masses, m_{DY} , at different \sqrt{s} . The prediction is obtained from a calculation of MCatNLO+CAS3 using TMD distributions obtained with the PB-NLO-2018 Set2 parameters for the collinear distribution, but with different q_s values. We scan for each m_{DY} -bin q_s in steps of 0.1 to 0.3 GeV in the range $q_s =$

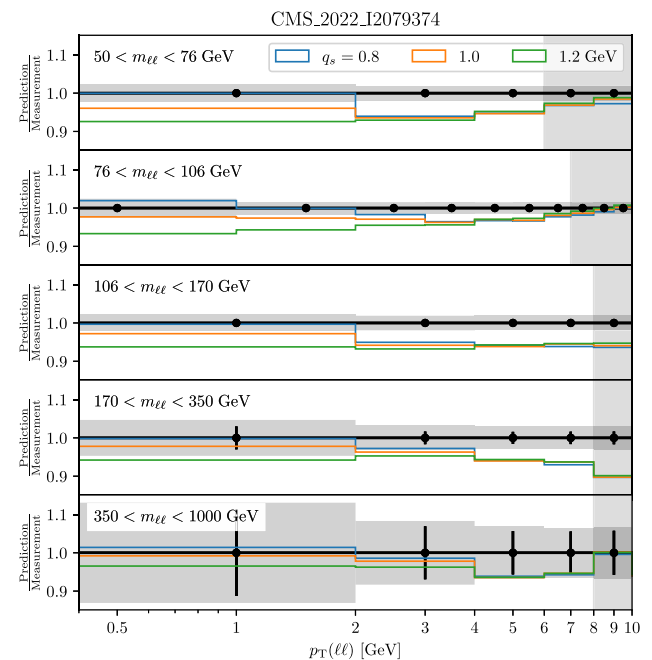


Fig. 7 Drell-Yan cross section ratios of MCatNLO+CAS3 predictions for different q_s values over CMS measurement [17] as a function of $p_T(\ell\ell)$ for different m_{DY} regions. Only the lowest $p_T(\ell\ell)$ values are shown. The points error bar show the statistical uncertainties and the gray bands the total experimental uncertainties. The gray area at the highest $p_T(\ell\ell)$ values show the maximal values included in the fit described in Sect. 3.2

0.1, . . . , 2.0 GeV. At higher DY transverse momenta, higher order contributions have to be taken into account (a study using multijet merging is given in Refs. [11,56,57]).

3.2 Fit of the Gauss width q_s in pp at $\sqrt{s} = 13$ TeV

The transverse momentum distribution of DY leptons has been measured by the CMS collaboration [17]. This is the basic measurement for the determination of the intrinsic- k_T

parameter q_s , since it covers a wide m_{DY} -range with high precision and that a detailed uncertainty breakdown, discussed in Sect. 3.2.1, is provided. The measurements of Z-production obtained from LHCb [58] are discussed in Sect. 3.2.2, while measurements at lower center-of-mass energies are shown in Sect. 3.3.

3.2.1 DY production over a wide DY mass range

The CMS collaboration has measured Drell–Yan production at 13 TeV [17] covering a range of DY mass $m_{DY} = [50, 76, 106, 170, 350, 1000]$ GeV. The measurement is provided with a detailed uncertainty breakdown, corresponding to a complete treatment of experimental uncertainties including correlations between bins of the measurement for each uncertainty source separately. Note that we use the fully detailed breakdown of the experimental uncertainties provided on the CMS public website.⁵

In order to determine the intrinsic- k_T we vary the q_s parameter and calculate a χ^2 to quantify the model agreement with the measurement. We evaluate the following expression,⁶

$$\chi^2 = \sum_{i,k} (m_i - \mu_i) C_{ik}^{-1} (m_k - \mu_k), \tag{8}$$

with m_i being the measurement and μ_i being the prediction for data point i . The covariance matrix C_{ik} is decomposed into a component describing the uncertainty in the measurement, $C_{ik}^{\text{meas.}}$, and the statistical and scale uncertainties in the prediction,

$$C_{ik} = C_{ik}^{\text{meas.}} + C_{ik}^{\text{model-stat.}} + C_{ik}^{\text{scale}}. \tag{9}$$

The covariance matrix of the measurement is taken directly from the supplementary material provided by CMS. The statistical uncertainty in the prediction, arising from the use of a Monte Carlo simulation, is accounted for as a small diagonal contribution without correlations between bins,

$$C_{ik}^{\text{model-stat.}} = \sigma_{i,\text{stat.}}^2 \delta_{ik}, \tag{10}$$

where $\sigma_{i,\text{stat.}}$ is the bin-by-bin statistical uncertainty. We also treat, for the first time, the scale uncertainties of the theoretical prediction as a correlated uncertainty, for a given m_{DY} range, allowing for a global shift of all bins together within the band defined by the symmetrized envelope of the scale uncertainties. This contribution to the covariance matrix is constructed as follows,

$$C_{ik}^{\text{scale}} = \sigma_{i,\text{scale}} \sigma_{k,\text{scale}}, \tag{11}$$

⁵ The corresponding HEPdata records only contain summarised information.

⁶ The code used with the full covariance matrix is available in Ref. [59], an earlier version to be used directly with Rivet is in Ref. [60].

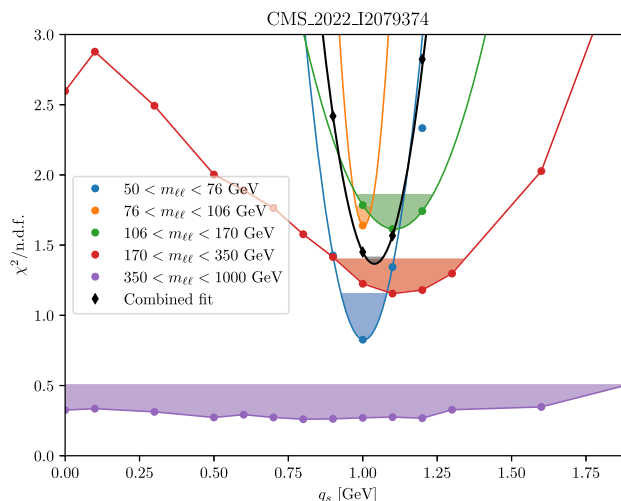


Fig. 8 The reduced $\chi^2/n.d.f.$ distribution as a function of q_s for different m_{DY} regions obtained from a comparison of the MCatNLO+CAS3 prediction with the measurement by CMS [17]. The points represent the obtained χ^2 values. The lines represent the curves used for the uncertainty estimate (see text), which is materialized by the shaded areas

where $\sigma_{i,\text{scale}}$ encodes the scale variation for each bin.

We first extract independent values of q_s for each invariant mass region considered in the measurement, considering only the region most sensitive to q_s , $p_T(\ell\ell) < 8$ GeV. We reduce this range further in the first two regions to $p_T(\ell\ell) < 6$ GeV for $50 < m_{DY} < 76$ GeV and $p_T(\ell\ell) < 7$ GeV for $76 < m_{DY} < 106$ GeV to stay in the region of sensitivity and not be biased by missing higher orders in the predictions affecting high $p_T(\ell\ell)$ shape. The obtained $\chi^2/n.d.f.$ (reduced χ^2) values are shown in Fig. 8 as a function of q_s .

Within each region, we consider the value of q_s for which the smallest χ^2 is obtained as our “best fit” value. We construct a one-sigma confidence region as the set of all q_s values for which $\chi^2(q_s) < \min(\chi^2) + 1$. When possible, this region is determined graphically using a linear interpolation between scan points. When the minimum is too narrow for a reliable determination of the uncertainty using this method, we use instead a quadratic interpolation between the lowest three points and add an uncertainty equal to one half-bin-width (0.05 GeV) in quadrature. In addition, we include an uncertainty derived by repeating the procedure with modified fit boundaries. The values obtained using this method are listed in Table 1 and a comparison is shown in Fig. 9.

The values derived from each m_{DY} interval are compatible with each other. The most precise determination is obtained from the Z peak region, $76 < m_{DY} < 106$ GeV, followed by the regions around it. The sensitivity at high mass suffers from larger statistical uncertainties in the measurement. This independence of the intrinsic- k_T with the DY mass contrasts with the need to tune the Parton Shower parameters for different masses in standard Monte Carlo events

generators (see [17] - Fig. 6 for a data comparison with MADGRAPH5_AMC@NLO interfaced with PYTHIA Parton Shower).

Having obtained compatible results, we proceed to deriving a combined fit by calculating a joint χ^2 including the considered bins in all mass ranges. For this, we construct a new covariance matrix $C_{ik}^{comb.}$ as a sum over the 650 uncertainty sources included in the detailed breakdown. We consider that each systematic uncertainty is fully correlated between m_{DY} regions and construct their covariance matrices in the same way as in Eq. (11). The statistical uncertainties (data and Monte Carlo) in the measurement feature nontrivial correlations due to the use of unfolding but are independent in each m_{DY} region, and therefore we construct a block-diagonal matrix from the covariance matrices in each m_{DY} region. The statistical uncertainty in the prediction is diagonal. We consider that the uncertainties in the QCD scales are not correlated between m_{DY} regions and use a block-diagonal matrix.

The χ^2 values obtained using the combined covariance matrix are shown in Fig. 8. The best fit value, extracted in the same way as for separate regions, is,

$$q_s = 1.04 \pm 0.03(\text{data}) \pm 0.05(\text{scan}) \pm 0.05(\text{binning}) \text{ GeV}.$$

This value and its uncertainty are shown as a black line and shaded area on Fig. 9 for comparison with the individual m_{DY} bins. A cross-check has been performed by interpolating the prediction for each bin between q_s values and searching for the minimum of the χ^2 distribution using a finer q_s grid. It returned values within the uncertainties quoted above. The TMD distributions including the new q_s value are available in TMDlib and TMDplotter [38, 39].

To make consistency checks of the obtained value of q_s and to examine possible trends of its dependence on DY mass and centre-of mass energy, the DY measurements at high rapidity and lower collision energies have been analysed. Since for these measurements no full error breakdown are available, we treat all uncertainties as being uncorrelated and do not include systematic uncertainty coming from the scale variation in the theoretical calculation.

Table 1 Results of the fit on individual m_{DY} intervals for the CMS measurement [17]. The “data” uncertainty is the one estimated using $\min(\chi^2) + 1$, the “scan” uncertainty accounts for the step size of the

m_{DY} region	Best χ^2	n.d.f	Best fit q_s [GeV]
50–76 GeV	2.45	3	$1.00 \pm 0.08(\text{data}) \pm 0.05(\text{scan}) \pm 0.1(\text{bins})$
76–106 GeV	11.4	7	$1.03 \pm 0.03(\text{data}) \pm 0.05(\text{scan}) \pm 0.05(\text{bins})$
106–170 GeV	6.46	4	$1.11 \pm 0.13(\text{data}) \pm 0.05(\text{scan}) \pm 0.2(\text{bins})$
170–350 GeV	4.62	4	$1.1^{+0.24}_{-0.18}(\text{data})$
350–1000 GeV	1.04	4	< 1.9

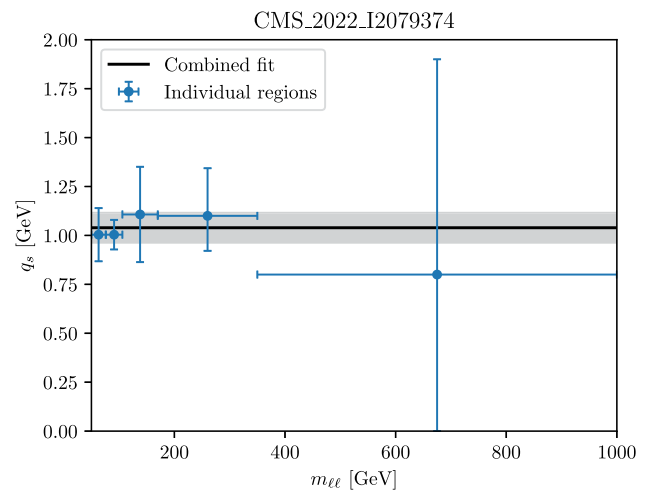


Fig. 9 The values of q_s in each m_{DY} -bin as obtained from Ref. [17]. Indicated is also the combined fit value of q_s

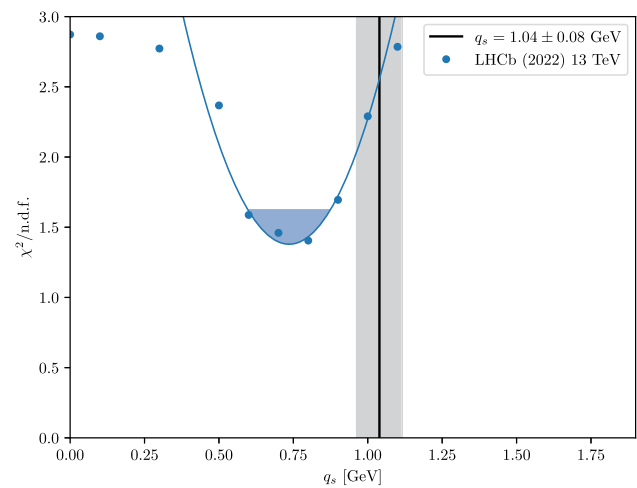


Fig. 10 The reduced $\chi^2/\text{n.d.f}$ distribution as a function of q_s summed over all rapidity regions obtained from a comparison of the MCatNLO+CAS3 prediction with the measurement by LHCb [58]. The shaded area corresponds to $\chi^2 + 1$. The best fit value is $q_s = 0.74 \pm 0.15$ GeV. The value of $q_s = 1.04 \pm 0.08$ GeV as obtained from the measurements in Ref. [17] is indicated by a black vertical line

q_s scan, and the “bins” uncertainty is derived by varying the number of bins included in the fit. The number of bins used in the fit gives n.d.f

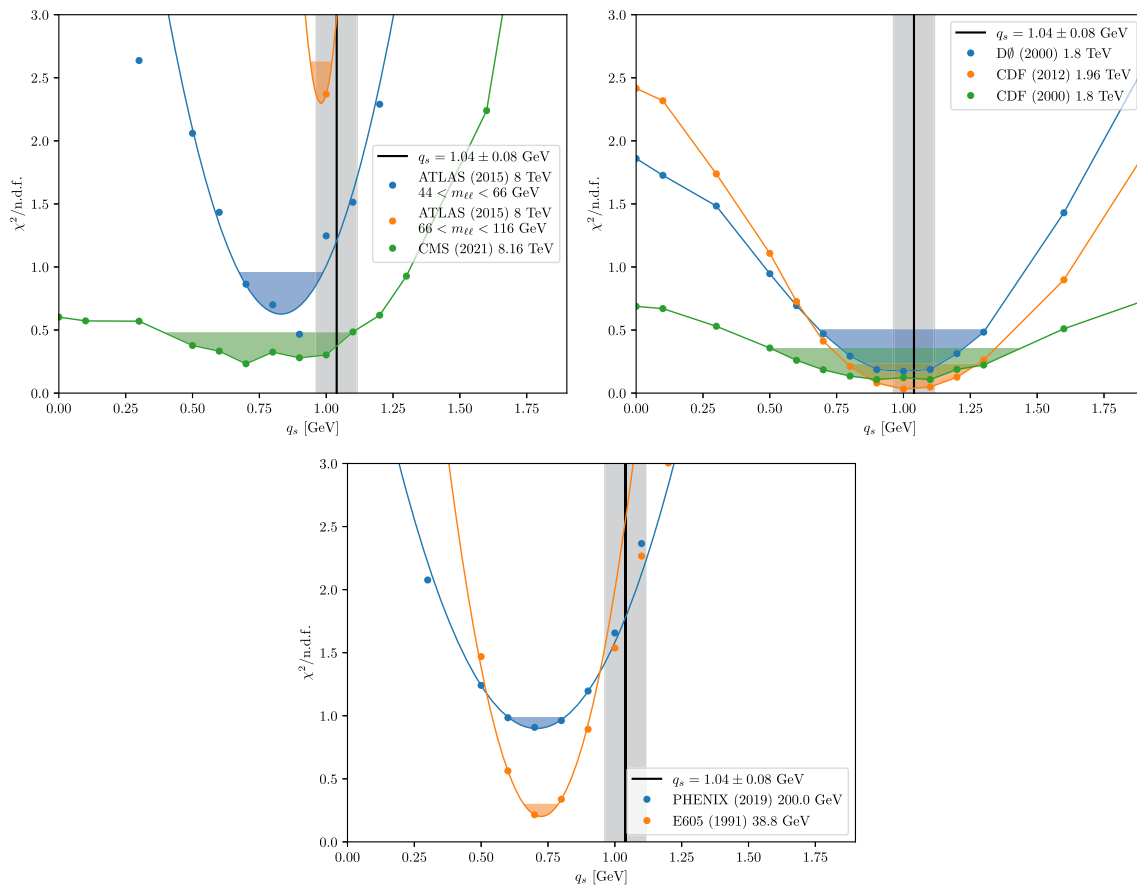


Fig. 11 The reduced $\chi^2/\text{n.d.f.}$ distribution as a function of q_s obtained from a comparison of the MCatNLO+CAS3 PB-NLO-2018 Set2 prediction with the measurements at lower center-of-mass energies. The colored shaded band shows the χ^2 variation of one unit for each data set. The value of $q_s = 1.04 \pm 0.08$ GeV is shown as the grey band. **Left-top:** ATLAS measurement in 2 mass bins that we anal-

ysed at $\sqrt{s} = 8$ TeV (n.d.f. = 4 for each mass bin) [61] and CMS in pPb at $\sqrt{s} = 8.1$ TeV [67]. **Right-top:** Tevatron measurements - D0 at $\sqrt{s} = 1.8$ TeV (n.d.f. = 4) [62], CDF at $\sqrt{s} = 1.8$ TeV (n.d.f. = 5) [63] and $\sqrt{s} = 1.96$ TeV (n.d.f. = 6) [64] **Bottom:** Measurements at lower energies - PHENIX at $\sqrt{s} = 200$ GeV (n.d.f. = 12) [65] and E605 at $\sqrt{s} = 38.8$ GeV (n.d.f. = 11) [66]

3.2.2 Z production at high rapidities at 13 TeV

The LHCb collaboration [58] has measured Z-production at $\sqrt{s} = 13$ TeV in the forward region, covering a rapidity range of $2 < |y| < 4.5$.

The χ^2 distribution is shown in Fig. 10 summed over the rapidity range of the DY lepton pair as a function of q_s . A minimum is obtained for $q_s = 0.74 \pm 0.15$ GeV, where the uncertainty comes from a variation of χ^2 by one unit and from the step size of the q_s scan.

3.3 The Gauss widths q_s from lower center of mass energies

The ATLAS collaboration has measured the production of DY from collisions at $\sqrt{s} = 8$ TeV in several DY mass bins, out of which only the two with $44 < m_{\text{DY}} < 66$ GeV and $66 < m_{\text{DY}} < 116$ GeV are relevant for $p_{\text{T}}(\ell\ell) < 10$ GeV

[61]. In Fig. 11 we show the $\chi^2/\text{n.d.f.}$ as a function of q_s obtained from these two mass bins (n.d.f = 8).

The Tevatron experiments D0 [62] and CDF have measured transverse momenta of DY lepton pairs created in $p\bar{p}$ collisions at lower center-of-mass energies (1.8 TeV [63] and 1.96 TeV [64]). The PHENIX collaboration measured DY production at $\sqrt{s} = 200$ GeV [65], and E605 [66] at $\sqrt{s} = 38.8$ GeV. The Drell–Yan differential cross section in $p_{\text{T}}(\ell\ell)$ has also been measured in pPb data at $\sqrt{s} = 8.1$ TeV by CMS [67]. Figure 11 shows the impact that the q_s choice has on $\chi^2/\text{n.d.f.}$ for these different measurements.

3.4 Consistency between determinations of intrinsic k_{T} width

A global fit of q_s is obtained by calculating χ^2 for different measurements, as shown in Table 2, including the corresponding center-of-mass energies, collision types and the

Table 2 All data sets with the corresponding center-of-mass energies, collision types and the number of degrees of freedom used for the global fit of q_s

Analysis	\sqrt{s}	Collision types	n.d.f
CMS_2022_I2079374 [17]	13 TeV	pp	25
LHCb_2022_I1990313 [58]	13 TeV	pp	5
CMS_2021_I1849180 [67]	8.1 TeV	pPb	5
ATLAS_2015_I1408516 [61]	8 TeV	pp	8
CDF_2012_I1124333 [64]	1.96 TeV	p \bar{p}	6
CDF_2000_S4155203 [63]	1.8 TeV	p \bar{p}	5
DO_2000_I503361 [62]	1.8 TeV	p \bar{p}	4
PHENIX_2019_I1672015 [65]	200 GeV	p \bar{p}	12
E605_1991_I302822 [66]	38.8 GeV	pp	11
Total			81

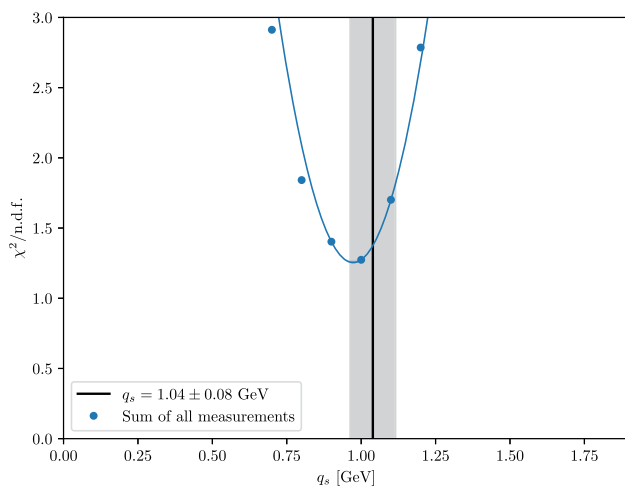


Fig. 12 The reduced $\chi^2/n.d.f.$ distribution (n.d.f. = 81) as a function of q_s obtained from a comparison of the MCatNLO+CAS3 PB-NLO-2018 Set2 prediction with the measurement of Refs. [17,58,61–67]. The minimum of global DY data fit is close to $q_s = 1$ GeV and consistent with the CMS measurement [17] shown separately by a black line

number of fitted data points, resulting in a total of 81 data points.

The impact of intrinsic- k_T distribution at lower collision energies has been analyzed using the entire range of $p_T(\ell\ell)$, while at higher center-of-mass energies we investigate up to the peak region in the transverse momentum distribution.

The $\chi^2/n.d.f.$ distribution as a function of q_s , for all the data together, is shown in Fig. 12. The χ^2 distribution exhibits a minimum at around $q_s = 1.0$ GeV, which is consistent with the value obtained as described above.

Figure 13 displays the value of q_s as a function of m_{DY} and \sqrt{s} obtained from the different measurements in Refs. [17,58,61–67]. For the data which do not provide detailed uncertainty breakdown and are mainly used for the cross checks and comparison purpose, the uncertainty bars of q_s shown in the figures are obtained from the χ^2 variation

of one unit and step size of the q_s scan only. The value of $q_s = 1.04 \pm 0.08$ GeV as derived from the measurements in Ref. [17], is compatible for all ranges of m_{DY} , and also holds true for various values of \sqrt{s} . The obtained value is also found to be compatible for pPb data.

To summarize, we have obtained a value for the width of the Gauss distribution for modeling the intrinsic- k_T distribution inside protons of $q_s = 1.04 \pm 0.08$ GeV. This value, in contrast to standard Monte Carlo event generators, has no strong dependence on the center-of-mass energy as well as on the mass of the produced Drell–Yan lepton pair m_{DY} . The results of this section indicate that the treatment of soft emissions in the region $z_{dyn} \lesssim z < z_M$ with the strong coupling of Eq. (6) applied in PB-NLO-2018 Set2 leads to intrinsic- k_T distributions with width parameter q_s consistent with Fermi motion kinematics, and mildly varying with energy.

4 Conclusion

In this paper we have carried out a detailed application of the PB-TMD methodology, which is reviewed in the first part of the paper, and used it to describe the DY low transverse momentum distributions across a wide range of DY masses. Within this methodology, we have presented the extraction of the intrinsic- k_T nonperturbative TMD parameter from fits to the measurements of DY p_T differential cross sections performed recently at the LHC at $\sqrt{s} = 13$ TeV, for DY masses between 50 GeV and 1 TeV. We have compared this with extractions from other DY measurements at different center-of-mass energies and masses.

As shown previously, the measured DY cross section at low p_T favours a choice of the strong coupling α_s scale to be taken as the transverse momentum of each parton emission, as in angular-ordered CMW parton cascades. This corresponds to the TMD parton distribution set PB-NLO-2018 Set2. In this paper we use PB-NLO-2018 Set2 with “pre-confinement” scale q_0 of 1 GeV. The strong coupling is evaluated at the emitted transverse momentum q_T for emissions with $q_T > q_0$, populating the phase space region $z < z_{dyn}$ (where $z_{dyn} = 1 - q_0/|\mathbf{q}'|$, with $|\mathbf{q}'|$ being the scale of the branching), while it is evaluated at the semi-hard scale q_0 for emissions with $q_T \lesssim q_0$. The contribution to the Sudakov evolution from the parton branching in the phase space region $z < z_{dyn}$ gives the perturbative resummation of Sudakov logarithms, while the contribution from the parton branching in the phase space region $z_{dyn} \lesssim z < z_M$ gives the nonperturbative Sudakov form factor. Therefore the PB-NLO-2018 Set2 contains two sources of nonperturbative effects: i) the nonperturbative TMD distribution at low evolution scale μ_0 , and ii) the nonperturbative Sudakov form factor, specified by the “pre-confinement” scale prescription to continue the branching evolution to the infrared region

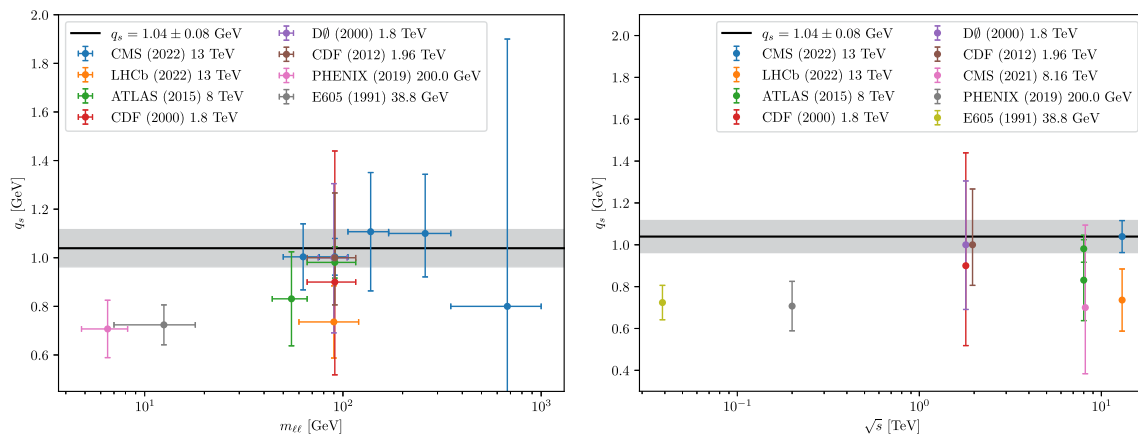


Fig. 13 Left: the value of q_s as a function of the DY-mass as obtained from the measurements in Refs. [17,58,61–67]. Right: same as a function of \sqrt{s} . The value of $q_s = 1.04 \pm 0.08$ GeV as obtained from the measurements in Ref. [17] is indicated

$z_{\text{dyn}} \lesssim z < z_M$. The former includes the intrinsic- k_T width parameter q_s , corresponding to Fermi motion in the hadron beam, while the latter is characterized by the semi-hard scale parameter q_0 . At low k_T , the contribution of nonperturbative Sudakov form factor interplays with the contribution of the intrinsic transverse momentum.

The main result of the present work is the extraction, within the PB-NLO-2018 Set2 framework, of the intrinsic- k_T Gauss distribution with zero mean and width parameter $q_s = \sqrt{2}\sigma$ from the measured p_T dependence of the DY cross sections obtained recently at the LHC at $\sqrt{s} = 13$ TeV [17], for different DY masses m_{DY} , between 50 GeV and 1 TeV. These measurements provide a complete decomposition of the different systematic uncertainties and their covariance matrices. To compare to the data, we have used DY production at NLO obtained with the MADGRAPH5_AMC@NLO event generator matched with the PB TMD distributions PB-NLO-2018 Set2, with a given parameter q_s value. We performed a scan over a large range of values q_s on the transverse momentum spectrum below the peak, i.e. the sensitive part to intrinsic- k_T , and considering separately each experimental source of uncertainty and their correlations. The theory scale uncertainties have been considered to be fully correlated inside each m_{DY} bin and uncorrelated between m_{DY} bins. We found the value $q_s = 1.04 \pm 0.08$ GeV, consistent for the different m_{DY} . The obtained value is in agreement to the expected value from Fermi-motion in protons. It has been cross checked that this value is compatible with q_s values obtained from other DY measurements at different center-of-mass energies \sqrt{s} and for a variety of DY masses. The global picture shows no strong dependence of the intrinsic- k_T on the center-of-mass energy or on the DY mass, which contrasts with tuned standard Monte Carlo event generators that need a strongly increasing intrinsic Gauss width with \sqrt{s} and with m_{DY} .

We suggest that the remarkably stable value of q_s that we obtain in our study can be attributed to the contribution of the nonperturbative Sudakov form factor and the treatment of the $z_{\text{dyn}} \lesssim z < z_M$ region near the soft-gluon resolution boundary.

Acknowledgements We are grateful to M. Abdullah Al-Mashad, L.I. Estevez Banos, L. Keersmaekers, A.M. van Kampen, K. Wichmann, Q. Wang, H. Yang from the CASCADE developer group for interesting and productive discussions. We are grateful to Louie Corpe for developing a code to calculate χ^2 including correlations within the Rivet frame. We also thank Marius Ambrozias for many discussions on the treatment of systematic uncertainties. This article is part of a project that has received funding from the European Union’s Horizon 2020 research and innovation programme under grant agreement STRONG 2020 - No 824093. LF is supported by the F.R.S.-FNRS of Belgium. A. L. acknowledges funding by Research Foundation-Flanders (FWO) (application number: 1272421N). LM acknowledges the support of the Deutsche Forschungsgemeinschaft (DFG, German Research Foundation) under Germany’s Excellence Strategy - EXC 2121 “Quantum Universe” - 390833306.

Data Availability Statement This manuscript has no associated data or the data will not be deposited. [Authors’ comment: The PB TMD grid files are stored for TMDlib (the source is available from <https://tmdlib.hepforge.org/>). The data grid files are available from the DESY cloud: <https://syncandshare.desy.de/index.php/s/ncL62ttzreJ83ZT.>]

Open Access This article is licensed under a Creative Commons Attribution 4.0 International License, which permits use, sharing, adaptation, distribution and reproduction in any medium or format, as long as you give appropriate credit to the original author(s) and the source, provide a link to the Creative Commons licence, and indicate if changes were made. The images or other third party material in this article are included in the article’s Creative Commons licence, unless indicated otherwise in a credit line to the material. If material is not included in the article’s Creative Commons licence and your intended use is not permitted by statutory regulation or exceeds the permitted use, you will need to obtain permission directly from the copyright holder. To view a copy of this licence, visit <http://creativecommons.org/licenses/by/4.0/>.

Funded by SCOAP³.

References

1. S. Drell, T.-M. Yan, Massive lepton pair production in hadron-hadron collisions at high-energies. *Phys. Rev. Lett.* **25**, 316 (1970)
2. J.C. Collins, D.E. Soper, G.F. Sterman, Transverse Momentum Distribution in Drell-Yan Pair and W and Z Boson production. *Nucl. Phys. B* **250**, 199 (1985)
3. T. Sjöstrand et al., An introduction to PYTHIA 8.2. *Comput. Phys. Commun.* **191**, 159 (2015). [arXiv:1410.3012](#)
4. J. Bellm et al., Herwig 7.0/Herwig++ 3.0 release note. *Eur. Phys. J. C* **76**, 196 (2016). [arXiv:1512.01178](#)
5. M. Bahr et al., Herwig++: physics and manual. *Eur. Phys. J. C* **58**, 639–707 (2008). [arXiv:0803.0883](#)
6. T. Gleisberg et al., Event generation with SHERPA 1.1. *JHEP* **0902**, 007 (2009). [arXiv:0811.4622](#)
7. A. Bermudez Martinez et al., Production of Z-bosons in the parton branching method. *Phys. Rev. D* **100**, 074027 (2019). [arXiv:1906.00919](#)
8. A. Bermudez Martinez et al., The transverse momentum spectrum of low mass Drell–Yan production at next-to-leading order in the parton branching method. *Eur. Phys. J. C* **80**, 598 (2020). [arXiv:2001.06488](#)
9. F. Hautmann et al., Collinear and TMD quark and gluon densities from Parton Branching solution of QCD evolution equations. *JHEP* **01**, 070 (2018). [arXiv:1708.03279](#)
10. F. Hautmann et al., Soft-gluon resolution scale in QCD evolution equations. *Phys. Lett. B* **772**, 446 (2017). [arXiv:1704.01757](#)
11. A. Bermudez Martinez, F. Hautmann, M. L. Mangano, TMD evolution and multi-jet merging. *Phys. Lett. B* **822**, 136700 (2021). [arXiv:2107.01224](#)
12. R. Angeles-Martinez et al., Transverse Momentum Dependent (TMD) parton distribution functions: status and prospects. *Acta Phys. Polon. B* **46**(12), 2501 (2015). [arXiv:1507.05267](#)
13. S. Gieseke, M. H. Seymour, A. Siodmok, A Model of non-perturbative gluon emission in an initial state parton shower. *JHEP* **06**, 001 (2008). [arXiv:0712.1199](#)
14. T. Sjöstrand, P. Skands, Multiple interactions and the structure of beam remnants. *JHEP* **03**, 053 (2004). [arXiv:hep-ph/0402078](#)
15. J. Isaacson, Y. Fu, C. P. Yuan, Improving ResBos for the precision needs of the LHC. [arXiv:2311.09916](#)
16. F. Hautmann, I. Scimemi, A. Vladimirov, Non-perturbative contributions to vector-boson transverse momentum spectra in hadronic collisions. *Phys. Lett. B* **806**, 135478 (2020). [arXiv:2002.12810](#)
17. CMS Collaboration, Measurement of the mass dependence of the transverse momentum of lepton pairs in Drell-Yan production in proton-proton collisions at $\sqrt{s} = 13$ TeV. *Eur. Phys. J. C* **83**(7), 628 (2023). [arXiv:2205.04897](#)
18. A. Bacchetta et al., Unpolarized Transverse Momentum Distributions from a global fit of Drell-Yan and Semi-Inclusive Deep-Inelastic Scattering data. [arXiv:2206.07598](#)
19. M. Bury et al., PDF bias and flavor dependence in TMD distributions. *JHEP* **10**, 118 (2022). [arXiv:2201.07114](#)
20. A. Bermudez Martinez et al., Collinear and TMD parton densities from fits to precision DIS measurements in the parton branching method. *Phys. Rev. D* **99**, 074008 (2019). [arXiv:1804.11152](#)
21. H. Jung, S. T. Monfared, T. Wening, Determination of collinear and TMD photon densities using the Parton Branching method. *Phys. Lett. B* **817**, 136299 (2021). [arXiv:2102.01494](#)
22. H. Jung, S. T. Monfared, TMD parton densities and corresponding parton showers: the advantage of four- and five-flavour schemes. [arXiv:2106.09791](#)
23. A. Bermudez Martinez et al., The transverse momentum spectrum of low mass Drell–Yan production at next-to-leading order in the parton branching method. *Eur. Phys. J. C* **80**, 598 (2020). [arXiv:2001.06488](#)
24. J. Alwall et al., The automated computation of tree-level and next-to-leading order differential cross sections, and their matching to parton shower simulations. *JHEP* **1407**, 079 (2014). [arXiv:1405.0301](#)
25. H. Yang et al., Back-to-back azimuthal correlations in Z+jet events at high transverse momentum in the TMD parton branching method at next-to-leading order. *Eur. Phys. J. C* **82**, 755 (2022). [arXiv:2204.01528](#)
26. F. Hautmann et al., A parton branching with transverse momentum dependent splitting functions. *Phys. Lett. B* **833**, 137276 (2022). [arXiv:2205.15873](#)
27. B.R. Webber, Monte Carlo Simulation of Hard Hadronic Processes. *Ann. Rev. Nucl. Part. Sci.* **36**, 253 (1986)
28. G. Marchesini, B.R. Webber, Monte Carlo Simulation of General Hard Processes with Coherent QCD Radiation. *Nucl. Phys. B* **310**, 461 (1988)
29. S. Catani, B.R. Webber, G. Marchesini, QCD coherent branching and semiinclusive processes at large x. *Nucl. Phys. B* **349**, 635 (1991)
30. V. N. Gribov, L. N. Lipatov, Deep inelastic ep scattering in perturbation theory. *Sov. J. Nucl. Phys.* **15**, 438 (1972). [*Yad. Fiz.*15,781(1972)]
31. L. N. Lipatov, The parton model and perturbation theory. *Sov. J. Nucl. Phys.* **20**, 94 (1975). [*Yad. Fiz.*20,181(1974)]
32. G. Altarelli, G. Parisi, Asymptotic freedom in parton language. *Nucl. Phys. B* **126**, 298 (1977)
33. Y. L. Dokshitzer, Calculation of the structure functions for Deep Inelastic Scattering and e^+e^- annihilation by perturbation theory in Quantum Chromodynamics. *Sov. Phys. JETP* **46**, 641 (1977). [*Zh. Eksp. Teor. Fiz.*73,1216(1977)]
34. F. Hautmann, L. Keersmaekers, A. Lelek, A. M. Van Kampen, Dynamical resolution scale in transverse momentum distributions at the LHC. *Nucl. Phys. B* **949**, 114795 (2019). [arXiv:1908.08524](#)
35. ZEUS, H1 Collaboration, Combination of measurements of inclusive deep inelastic $e^\pm p$ scattering cross sections and QCD analysis of HERA data. *Eur. Phys. J. C* **75**, 580 (2015). [arXiv:1506.06042](#)
36. xFitter Developers' Team Collaboration, H. Abdolmaleki et al., xFitter: An Open Source QCD Analysis Framework. A resource and reference document for the Snowmass study. **6** (2022). [arXiv:2206.12465](#)
37. S. Alekhin et al., HERAFitter, Open Source QCD Fit Project. *Eur. Phys. J. C* **75**, 304 (2015). [arXiv:1410.4412](#)
38. F. Hautmann et al., TMDlib and TMDplotter: library and plotting tools for transverse-momentum-dependent parton distributions. *Eur. Phys. J. C* **74**(12), 3220 (2014). [arXiv:1408.3015](#)
39. N. A. Abdulov et al., TMDlib2 and TMDplotter: a platform for 3D hadron structure studies. *Eur. Phys. J. C* **81**, 752 (2021). [arXiv:2103.09741](#)
40. M. I. Abdulhamid et al., Azimuthal correlations of high transverse momentum jets at next-to-leading order in the parton branching method. *Eur. Phys. J. C* **82**, 36 (2022). [arXiv:2112.10465](#)
41. D. Amati et al., A treatment of hard processes sensitive to the infrared structure of QCD. *Nucl. Phys. B* **173**, 429 (1980)
42. A. Bassetto, M. Ciafaloni, G. Marchesini, Jet structure and infrared sensitive quantities in perturbative QCD. *Phys. Rept.* **100**, 201–272 (1983)
43. A. M. van Kampen, Drell-Yan transverse spectra at the LHC: A comparison of parton branching and analytical resummation approaches. *SciPost Phys. Proc.* **8**, 151 (2022). [arXiv:2108.04099](#)
44. A. Bermudez Martinez et al. to be published
45. H. Jung et al., The Parton Branching evolution for collinear and TMD parton densities - uPDFevolv2. to be published, 2023
46. Z. Nagy, D. E. Soper, Evolution of parton showers and parton distribution functions. *Phys. Rev. D* **102**(1), 014025 (2020). [arXiv:2002.04125](#)

47. S. Frixione, B. R. Webber, Correcting for cutoff dependence in backward evolution of QCD parton showers. [arXiv:2309.15587](#)
48. M. Mendizabal, F. Guzman, H. Jung, S. Taheri Monfared, On the role of soft gluons in collinear parton densities. [arXiv:2309.11802](#)
49. S. Baranov et al., CASCADE3 A Monte Carlo event generator based on TMDs. *Eur. Phys. J. C* **81**, 425 (2021). [arXiv:2101.10221](#)
50. T. Sjöstrand, S. Mrenna, P. Skands, PYTHIA 6.4 physics and manual. *JHEP* **05**, 026 (2006). [arXiv:hep-ph/0603175](#)
51. CMS Collaboration, Measurement of the differential Drell-Yan cross section in proton-proton collisions at $\sqrt{s} = 13$ TeV. *JHEP* **12**, 059 (2019). [arXiv:1812.10529](#)
52. A. Buckley et al., Rivet user manual. *Comput. Phys. Commun.* **184**, 2803 (2013). [arXiv:1003.0694](#)
53. CMS Collaboration, Measurements of differential Z boson production cross sections in proton-proton collisions at $\sqrt{s} = 13$ TeV. *JHEP* **12**, 061 (2019). [arXiv:1909.04133](#)
54. ATLAS Collaboration, Measurement of the low-mass Drell-Yan differential cross section at $\sqrt{s} = 7$ TeV using the ATLAS detector. *JHEP* **06**, 112 (2014). [arXiv:1404.1212](#)
55. CMS Collaboration, Study of Final-State Radiation in Decays of Z Bosons Produced in pp Collisions at 7 TeV. *Phys. Rev. D* **91**, 092012 (2015). [arXiv:1502.07940](#)
56. A. Bermudez Martinez, F. Hautmann, M. L. Mangano, Multi-jet merging with TMD parton branching. *JHEP* **09**, 060 (2022). [arXiv:2208.02276](#)
57. A. Bermudez Martinez, F. Hautmann, M. L. Mangano, Multi-jet physics at high-energy colliders and TMD parton evolution (2021). [arXiv:2109.08173](#)
58. LHCb Collaboration, Precision measurement of forward Z boson production in proton-proton collisions at $\sqrt{s} = 13$ TeV. *JHEP* **07**, 026 (2022). [arXiv:2112.07458](#)
59. L. Moureaux, I. Bujanja, Fits with covariance matrices. <https://github.com/lmoureaux/CovarianceFits>
60. L. Corpe, *Correlations Library* (Jet and electroweak bosons, Contribution to yellow report of LHCEW working group, 2019)
61. ATLAS Collaboration, Measurement of the transverse momentum and ϕ_{η}^* distributions of Drell-Yan lepton pairs in proton-proton collisions at $\sqrt{s} = 8$ TeV with the ATLAS detector. *Eur. Phys. J. C* **76**, 291 (2016). [arXiv:1512.02192](#)
62. D0 Collaboration, Measurement of the inclusive differential cross section for Z bosons as a function of transverse momentum in $p\bar{p}$ collisions at $\sqrt{s} = 1.8$ TeV. *Phys. Rev. D* **61**, 032004 (2000). [arXiv:hep-ex/9907009](#)
63. CDF Collaboration, The transverse momentum and total cross section of e^+e^- pairs in the Z boson region from $p\bar{p}$ collisions at $\sqrt{s} = 1.8$ TeV. *Phys. Rev. Lett.* **84**, 845 (2000). [arXiv:hep-ex/0001021](#)
64. CDF Collaboration, Transverse momentum cross section of e^+e^- pairs in the Z-boson region from $p\bar{p}$ collisions at $\sqrt{s} = 1.96$ TeV. *Phys. Rev. D* **86**, 052010 (2012). [arXiv:1207.7138](#)
65. PHENIX Collaboration, Measurements of $\mu\mu$ pairs from open heavy flavor and Drell-Yan in $p + p$ collisions at $\sqrt{s} = 200$ GeV. *Phys. Rev. D* **99**, 072003 (2019). [arXiv:1805.02448](#)
66. G. Moreno et al., Dimuon production in proton - copper collisions at $\sqrt{s} = 38.8$ GeV. *Phys. Rev. D* **43**, 2815 (1991)
67. CMS Collaboration, Study of Drell-Yan dimuon production in proton-lead collisions at $\sqrt{s_{NN}} = 8.16$ TeV. *JHEP* **05**, 182 (2021). [arXiv:2102.13648](#)